The evolution of Griffiths-phase-like features and colossal magnetoresistance in $La_{1-x}Ca_xMnO_3$ ($0.18 \leq x \leq 0.27$) across the compositional metal–insulator boundary

2009 J. Phys.: Condens. Matter 21 415603

(http://iopscience.iop.org/0953-8984/21/41/415603)

J. Phys.: Condens. Matter **21** (2009) 415603 (15pp) doi:10.1088/0953-8984/21/41/415603

The evolution of Griffiths-phase-like features and colossal magnetoresistance in $La_{1-x}Ca_xMnO_3$ ($0.18 \leqslant x \leqslant 0.27$) across the compositional metal–insulator boundary

Wanjun Jiang[1], XueZhi Zhou[1], Gwyn Williams[1], Y Mukovskii[2] and R Privezentsev[2]

[1] Department of Physics and Astronomy, University of Manitoba, Winnipeg, MB, R3T 2N2, Canada
[2] State Technological University 'Moscow Steel and Alloys Institute' (MISIS), Moscow 119049, Russia

E-mail: jiang@physics.umanitoba.ca

Received 20 July 2009, in final form 30 August 2009
Published 24 September 2009
Online at stacks.iop.org/JPhysCM/21/415603

Abstract

Detailed measurements of the magnetic and transport properties of single crystals of $La_{1-x}Ca_xMnO_3$ ($0.18 \leqslant x \leqslant 0.27$) are summarized, and lead to the following conclusions. While temperature-dependent (magneto-) resistance measurements narrow the compositionally modulated metal–insulator (M–I) transition to lie between $0.19 \leqslant x_c \leqslant 0.20$ in the series studied, comparisons between the latter magnetic data provide the first unequivocal demonstration that (i) the presence of Griffiths-phase-like (GP) features do not guarantee colossal magnetoresistance (CMR), while confirming (ii) that neither are the appearance of such features a prerequisite for CMR. These data also reveal that (iii) whereas continuous magnetic transitions occur for $0.18 \leqslant x \leqslant 0.25$, the universality class of these transitions belongs to that of a nearest-neighbour 3D Heisenberg model only for $x \leqslant 0.20$, beyond which complications due to GP-like behaviour occur. The implications of the variation (or lack thereof) in critical exponents and particularly critical amplitudes and temperatures across the compositionally mediated M–I transition support the assertion that the dominant mechanism underlying ferromagnetism across the M–I transition changes from ferromagnetic super-exchange (SE) stabilized by orbital ordering in the insulating phase to double-exchange (DE) in the orbitally disordered metallic regime. The variations in the acoustic spin-wave stiffness, D, and the coercive field, H_C, support this conclusion. These SE and DE interaction mechanisms are demonstrated to not only belong to the same universality class but are also characterized by comparable coupling strengths. Nevertheless, their percolation thresholds are manifestly different in this system.

(Some figures in this article are in colour only in the electronic version)

1. Introduction

Transition metal oxides exhibit fascinating properties; these include multiferroicity, superconductivity, and colossal magnetoresistance (CMR) [1–3]. Many of these appear to be critically sensitive to differing types/levels of ion substitutions; for example, varying the Sr substitution level in the $La_{1-x}Sr_xCuO_4$ cuprate system can induce a superconducting, antiferromagnetic (AFM) or non-Fermi liquid state [2]. Other striking examples occur in CMR perovskite manganites [3–7];

here, dramatic changes in resistivity result from a metal–insulator (M–I) transition, the temperature of which exhibits a marked field dependence—the latter often occurring in close proximity to a paramagnetic–ferromagnetic (PM–FM) transition. Such CMR materials are often characterized by the general formula $(A^{3+})_{1-x}(B^{2+})_x(Mn^{4+})_{1-x}(Mn^{3+})_x(O^{2-})_3$, A being a trivalent rare-earth ion (i.e. La, Nd, Pr, etc) and B a divalent alkaline earth cation (i.e. Ba, Ca, Sr, etc) which substitutes randomly at the trivalent rare-earth ion A sites. The substitution/doping level, x, modulates the valence state of the Mn ions (the ratio of Mn^{4+}/Mn^{3+} is proportional to $x/(1-x)$) in order to maintain charge neutrality. The accompanying mismatch in the ionic size of ions occupying the A site leads to a distortion in the crystal structure frequently characterized by the average A-site radius, $\langle r_A\rangle$, the variance, $\sigma = (\langle r_A^2\rangle - \langle r_A\rangle^2)^{1/2}$, in the A-site radii and the 'tolerance factor', $t_f = [\langle r_A\rangle + r_O]/(\sqrt{2}[\langle r_{Mn}\rangle + r_O])$, here $\langle r_{Mn}\rangle$ and r_O are the average radii of the Mn and O sites, respectively [8, 9]. For different doping levels and with varying ionic radii accompanying substitution, distortions occur, with the crystal structure transforming from being initially nearly cubic perovskite ($t_f \approx 1$), through rhombohedral ($0.96 < t_f < 1$), to an orthorhombic ($t_f < 0.96$) structure [5–7]. This is accompanied by reductions in the Mn–O–Mn bond angle below the 'ideal' value of 180°, thus changing the charge transfer integral (t_{eff}), a process that can lead to the charge localization [10, 11].

Below we present a study of single-crystal $La_{1-x}Ca_xMnO_3$ with $0.18 \leqslant x \leqslant 0.27$, encompassing the compositionally driven M–I transition boundary region, $0.18 \leqslant x_c \leqslant 0.22$ [12], where many of the above-mentioned effects are important.

Prior to a discussion of the implications of these data, a brief review of the relevant background is in order. The appearance of CMR in manganites was initially considered within the framework of a spin-dependent double-exchange (DE) model [10] in which FM interactions between the localized Mn t_{2g} spins are mediated by the hopping of itinerant e_g spins, summarized by the charge transfer integral $t_{eff} = t_0 \cos(\theta/2)$, where θ is the angle between the neighbouring t_{2g} core sites involved in the hopping process [10]. In particular, the onset of metallicity is linked with the establishment of an infinite (percolation) pathway of DE metallic bonds, the same bonds that establish an infinite FM 'backbone'; such an approach provided a qualitative explanation of the simultaneous appearance of metallicity and ferromagnetism—considered a fundamental strength of the DE approach. However, subsequent studies demonstrated that DE alone failed at a quantitative level, indicating further that contributions from the Jahn–Teller effect and the electron–phonon interaction needed to be included [13]. Later discussions have included the role of spontaneous electronic phase separation [14] and the relationship between the occurrence of a Griffiths-phase-like (GP) feature and CMR [15–17], amongst others; currently the physical mechanism underlying CMR remains controversial. That the emergence of FM and CMR are governed by percolative mechanisms appears generally agreed: however, questions have arisen recently as to whether they emerge coincidental. $Pr_{1-x}Ca_xMnO_3$ represents an extreme counterexample to the latter, exhibiting insulating behaviour over an extended temperature range at all doping levels in zero field [11], so that a percolative conducting pathway is never established. However, at moderate doping levels ($x \sim 0.27$–0.29), not only does a FM ground state emerge (indicating the establishment of an infinite, percolating FM backbone, but one obviously not DE-linked) but the universality class of the magnetic transition [18] is that of the nearest-neighbour 3D Heisenberg model [19]. The latter also characterizes metallic $La_{1-x}Ca_xMnO_3$ at a comparable composition ($x = 0.20$ [16]) and predicted for the DE model when anisotropy effects are not important [20, 21].

$La_{1-x}Ca_xMnO_3$ is regarded currently as a prototypical CMR system, exhibiting a complex phase diagram as a function of temperature and chemical substitution (x) [4–7]. Below $x = 0.125$, it exhibits a canted-AFM insulating ground state, which evolves into a FM insulating state as the doping level is increased to $0.125 \leqslant x \leqslant 0.18$. At still higher doping levels, $0.22 \leqslant x \leqslant 0.50$, an FM metallic state emerges, accompanied by CMR. In the so-called hole-doped regime, $0.50 \leqslant x \leqslant 0.85$, a charge-ordered (CO), AFM insulating states predominate, terminating as a canted-AFM insulating ground state in the doping range $0.85 \leqslant x \leqslant 1$. The present study focuses on the doping range $0.18 \leqslant x \leqslant 0.27$ where both ferromagnetism and metallicity first emerge, although not, as our detailed measurements confirm, coincidentally.

2. Experimental details

Measurements were carried out on a series of $La_{1-x}Ca_xMnO_3$ high quality single crystals (they displayed a mosaicity typically less than 1°) with the nominal compositions $x = 0.18$, 0.19, 0.20, 0.21, 0.23, 0.25 and 0.27, grown using the floating zone technique [22]. The (magneto-) resistivities, ($\rho(T, H)$), were acquired using a Model 7000 AC Transport Controller, and utilized a four-probe technique with an excitation current of 10 mA at 499 Hz. Contacts to samples with typical dimensions ($4 \times 1 \times 1$) mm^3 were made by compressing indium 'pads' over gold current/voltage wires embedded in grooves ground in the samples with a diamond wire saw. Measurements of the ac susceptibility, $\chi(T, H)$ (at 1 kHz with a driving field of 0.1 Oe rms), and of the magnetic isotherm, $M(T, H)$, at various temperatures, T, and fields, H, were carried out in a Quantum Design model 6000 physical property measurement system (PPMS) magnetometer/susceptometer, with all fields applied along the largest dimensions of similarly shaped samples to minimize demagnetization effects. Prior to measuring at any given temperature, the sample was demagnetized by warming to 300 K—well above the ordering temperature—and then cooling to a predetermined measuring temperature in zero field.

3. Experimental results and analyses

3.1. General features

From the magnetic isotherm measured at 2 K, estimates for the saturation magnetization M_{SAT} were obtained from extrapolations of M versus H^{-1} plots (not reproduced here); these estimates are consistent (within an experimental uncertainty of ∼1–2%) with the theoretical, spin-only values and the nominal compositions (table 1). As a corollary, no evidence supporting appreciable spin canting was found.

Figure 1 reproduces the temperature-dependent resistivities $\rho(T, H)$ measured in static magnetic fields of 0, 30 and 90 kOe; the insets display the associated magnetoresistance ($\Delta\rho = [\rho(0) - \rho(H)]/\rho(H)$). The narrow composition steps chosen in the present study indicate that, with but a 1% change in the Ca substitution level, specifically from $x = 0.19$ to 0.20, the ground state resistivities exhibit a dramatic decrease exceeding 10^4 [12]. Above $x = 0.20$ this system displays an M–I transition, the temperature of which increases with further increases in Ca substitution, with an attendant reduction in the associated peak resistivity and the accompanying magnetoresistance/CMR, $\Delta\rho$. Over the composition range studied here, the ratio of $\rho(10\ \mathrm{K}, 0)$ between insulating and metallic ground state approaches 10^6, consistent with a range of previous results [12, 23–32]. The nature of this insulating ground state remains controversial, a point returned to below.

To relate the general transport behaviour with the corresponding magnetic response, the results of zero-field ac susceptibility measurements are summarized in figure 2—the real part (χ) in figure 2(a) and the imaginary component (χ'') in figure 2(b). Despite their closeness in composition, these data exhibit marked differences, the most relevant of which—in terms of the current study—can be seen in figure 3, in which the inverse ac susceptibilities ($1/\chi$) (measured in both zero field and in various static biasing fields up to 1 kOe) are plotted as a function of temperature. The characteristic depression evident for some of these data below the higher-temperature Curie–Weiss line is symptomatic of so-called GP-like behaviour [15–17, 33], namely an inverse susceptibility of the form

$$\chi^{-1} \propto (T - T_C^{\mathrm{Rand}})^{1-\lambda}; \qquad \lambda < 0 < 1. \tag{1}$$

The occurrence of GP-like features have been reported in a range of doped perovskites based on various physical measurements [15–17, 34–40]; their presence has been attributed to the influence of disorder on the phase complexity in the manganites and related systems [38–41]. Briefly, in the original problem discussed by Griffiths [33], nearest-neighbour exchange bonds of strength J occurred with probability p, with disorder being represented via bonds of zero strength and probability $(1 - p)$. Below the percolation threshold, p_c, of the relevant lattice there is zero probability of establishing an infinite percolating 'backbone' (thus the correlation length does not diverge, in the context of continuous transitions). Cooperative ferromagnetism is therefore not established; neither, in the present context, is a

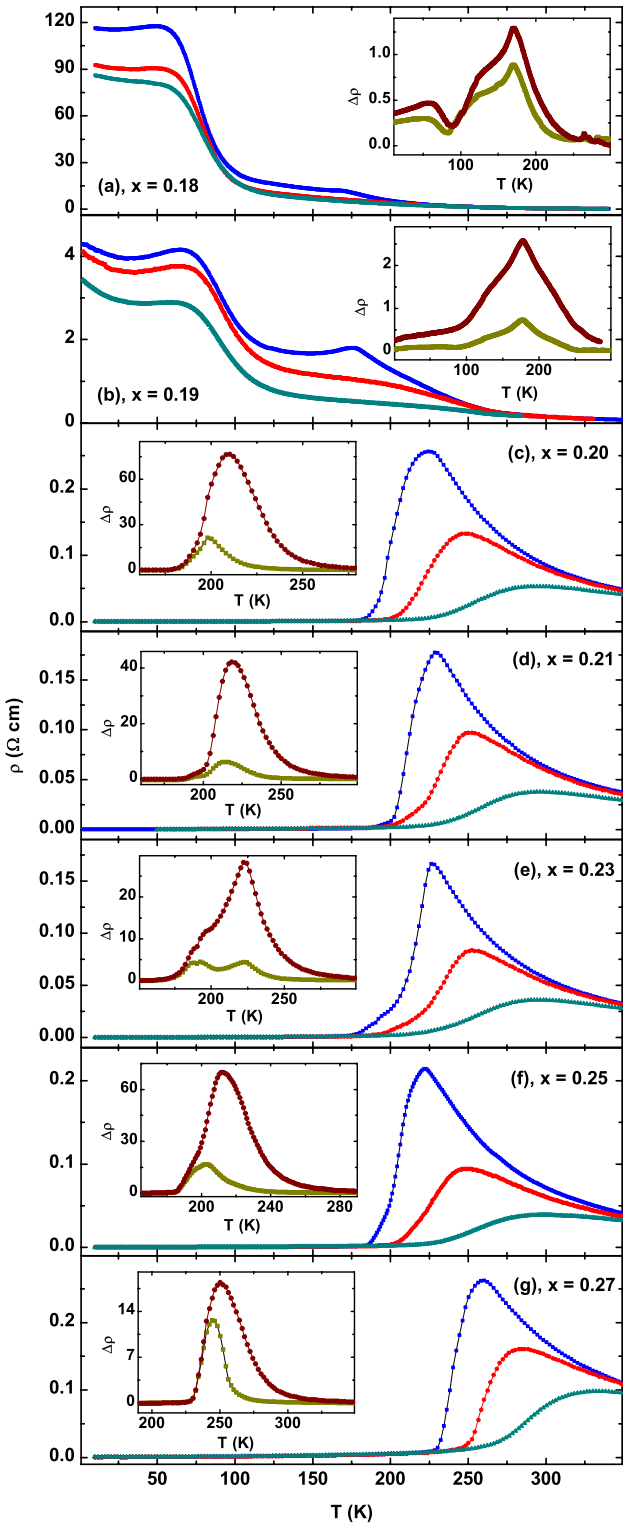

Figure 1. Main body, the temperature-dependent (magneto-) resistivity $\rho(T, H)$ under different static magnetic fields (0, 30, 90 kOe); measured on warming following zero-field cooling (ZFC). Insets show the magnetoresistance ($\Delta\rho = [\rho(0) - \rho(H)]/\rho(H)$). Figures (a) to (g) correspond to $x = 0.18$, 0.19, 0.20, 0.21, 0.23. 0.25 and 0.27, respectively.

DE-linked (and hence FM) pathway. In contrast, for $p > p_c$, FM order is established (and, by inference within the DE model, a percolating conducting network) but, as expected, at a

Table 1. Parameters characterizing single-crystal $La_{1-x}Ca_xMnO_3$ ($0.18 \leqslant x \leqslant 0.30$). Data of $x = 0.30$ are cited from [12] to [15]. '—' stands for no data available.

Composition	$x = 0.18$	$x = 0.19$	$x = 0.20$	$x = 0.21$	$x = 0.23$	$x = 0.25$	$x = 0.27$	$x = 0.30$
Structural properties								
$\langle r_A \rangle$ (Å)	1.2096	1.2092	1.2088	1.2084	1.2078	1.2072	1.2063	1.2051
Tolerance factor (t_f)	0.936 07	0.929 67	0.923 37	0.917 41	0.917 17	0.916 88	0.916 65	0.916 27
σ (Å)	0.0138	0.0141	0.0144	0.0147	0.0151	0.0156	0.0159	0.0165
Transport properties								
ρ ($T = 2$ K) (Ω cm)	120	4	1.72×10^{-4}	1.85×10^{-4}	1.79×10^{-4}	1.77×10^{-4}	1.82×10^{-4}	1.6×10^{-4}
E_a (meV)	161.2	160.8	135.8	135.3	132.7	126.9	119.2	—
ρ_0 (10^{-8} Ω cm $T^{-3/2}$)	20.5	13.7	8.3	6.8	5.6	4.2	3.1	—
Magnetic properties								
β	0.37	0.38	0.37	0.10	0.41	0.12	0.12	0.12
γ	1.38	1.34	1.38	1.65	1.35	1.62	1.63	1.63
δ	4.8	4.8	4.8	20	5.2	18	∼28	28
E (emu g^{-1} Oe^{-1})	5.4 ± 0.1	5.3 ± 0.1	5.2 ± 0.1					
T_C (K)	171	173	179	182	185	189	232	212
T_G (K)	No	256	No	252	232	224	275	232
GP	No	Yes	No	Yes	Yes	Yes	Yes	Yes
$M_S(0)$ (emu g^{-1})	94.45	90.92	91.87	90.71	91.24	92.75	89.05	—
M_{SAT} (emu g^{-1})	95.23	91.44	91.93	91.25	91.73	92.93	89.62	—
H_C (Oe)	35	36	12	10	9	7	6	—
D (meV $Å^2$)	65	62	65	120	118	123	126	160

temperature $T_C(p)$ below that of the undiluted system [$T_C(p = 1) = T_G$]. The temperature interval $T_C(p) < T < T_G$ defines the Griffiths regime; here the system response is neither simply PM/Curie–Weiss-like nor is an infinite percolating chain/divergent correlation length established; in this regime the response is dominated by the largest cluster/correlated volume, leading to the prediction for the inverse susceptibility given in equation (1). Whereas GP-like features have been shown to correlate closely with CMR in this system near optimal doping [15], a comparison of the data in figures 1 and 3 provide (i) further confirmation of the earlier conclusion [16] that GP-like features are *not* a prerequisite for CMR—the $x = 0.20$ and 0.21 samples both exhibit CMR, whereas only the latter displays GP-like features, and (ii) allows the important new caveat that the appearance of GP-like features does not *guarantee* the emergence of CMR—the $x = 0.19$ specimen exhibits GP-like features but has an insulating ground state and hence no appreciable magnetoresistance. Such conclusions notwithstanding, these data raise further questions regarding our current understanding of the fundamental mechanism(s) underlying CMR [16, 17], namely, the specific origin of the 'disorder' relevant to establishing GP-like characteristics in the present system. Unlike recent reports linking such characteristics with phase competition in optimally doped $(La_{1-y}Pr_y)_{0.7}Ca_{0.3}Mn^{16/18}O_3$ ($y \leqslant 0.85$) [38], no such definitive results exist currently for $La_{1-x}Ca_xMnO_3$. In general terms, however, it does not seem unlikely that oxygen stoichiometry may play some role through changes necessary to maintain charge neutrality, as summarized by

$$La^{3+}_{1-x}Ca^{2+}_{x}Mn^{3+}_{1-x+2\Delta}Mn^{4+}_{x-2\Delta}O^{2-}_{3-\Delta}. \tag{2}$$

One consequence of oxygen deficiency (represented by Δ) would be changes in the ratio of DE-linked Mn^{3+}–Mn^{4+} sites and the numbers of Mn^{3+}–Mn^{3+} and Mn^{4+}–Mn^{4+} super-exchange (SE) interactions [42, 43], influencing principally the distribution/disorder of exchange couplings. Unfortunately, no means of measuring the oxygen stoichiometry with sufficient precision to comment with the necessary degree of certainty on this issue in the present series of samples is currently available to us.

3.2. Detailed critical behaviour

3.2.1. Background. The conventional analysis of critical behaviour in the vicinity of a continuous PM–FM transition is based on the scaling law equation of state relating the reduced magnetization, $m(h, t)$, to the usual (reduced) linear scaling fields $t = (T - T_C)/T_C$ and $h \sim H_i/T_C$ (where the internal field $H_i = H_a - N_D M$, H_a being the applied field, N_D the demagnetization factor and M magnetization) [44], namely

$$m(h, t_m) = |t|^{\beta} F_{\pm}\left(\frac{h}{|t|^{\gamma+\beta}}\right) \tag{3}$$

in which $F_{\pm}(x)$ is the unspecified scaling function. Equation (3) leads to the following well-established power-law predictions along the critical isotherm ($T = T_C$, $t = 0$):

$$M(H, T = T_C) = M_0 H^{1/\delta}; \qquad m(h, 0) \sim E h^{1/\delta} \tag{4}$$

for the initial susceptibility [$\chi_i(T) = (\partial M/\partial H)_{H=0}$]:

$$\chi_i(T) = \chi_0\left(\frac{T}{T_C} - 1\right)^{-\gamma}; \qquad \chi_i(t) = \frac{\partial m}{\partial h} \sim C t^{-\gamma} \quad (T > T_C) \tag{5}$$

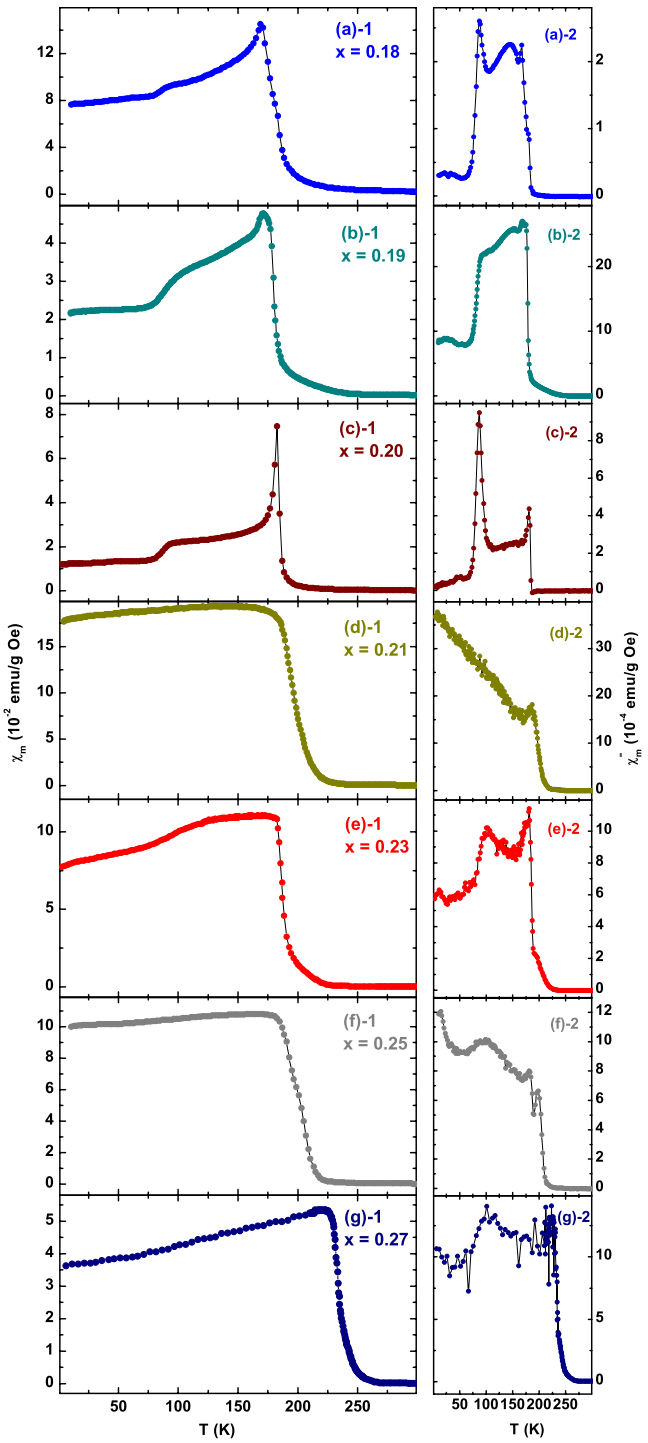

Figure 2. Figures (a)-1 to (g)-1 are the in-phase zero-field ac susceptibility to $x = 0.18$, 0.19, 0.20, 0.21, 0.23, 0.25 and 0.27, respectively, measured on warming following ZFC. Figures (a)-2 to (g)-2 are the corresponding imaginary components of ac susceptibility.

and for the (reduced) spontaneous magnetization $M_S(T) = M_S\ (H = 0, T)$:

$$M_S(T) = M_S(0)\left(1 - \frac{T}{T_C}\right)^{\beta}; \qquad m(0,t) \sim B|t|^{\beta} \quad (T < T_C). \tag{6}$$

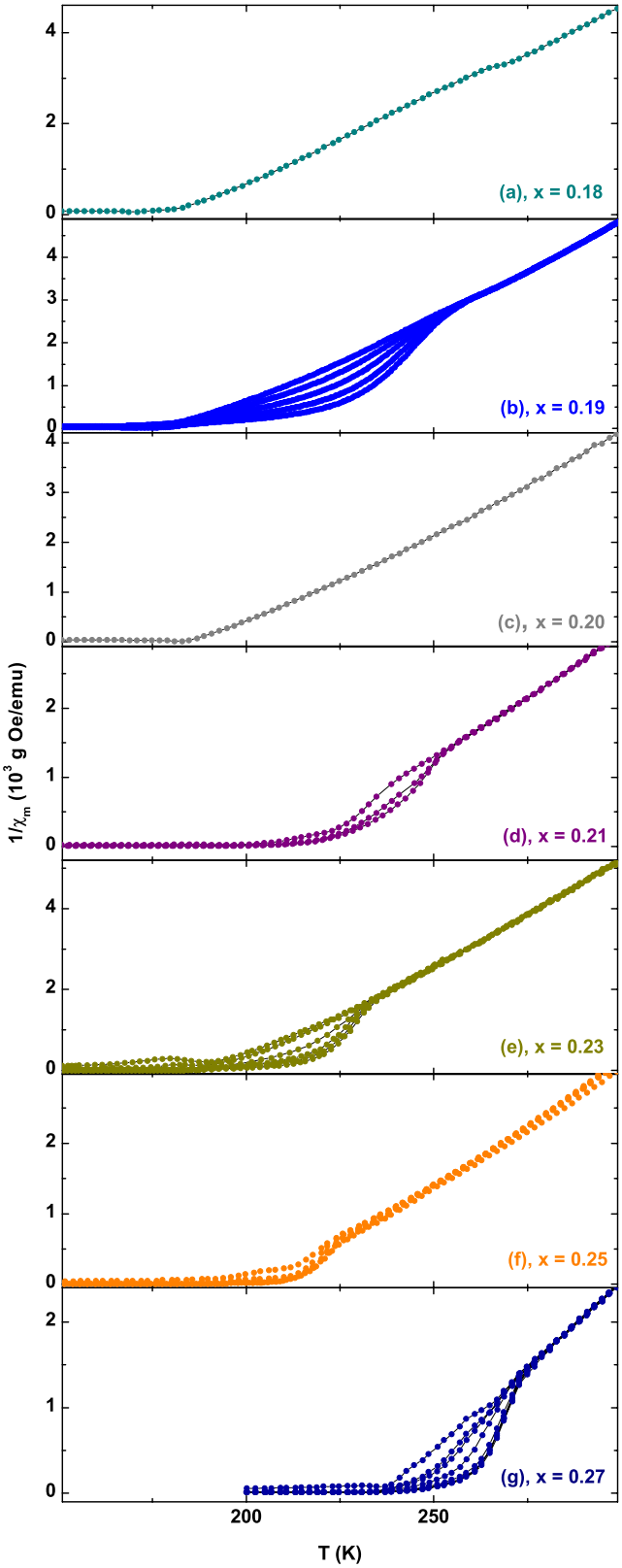

Figure 3. The inverse ac susceptibility measured under various static magnetic fields starting from zero field (bottom curve), figures (a) to (g) corresponding to $x = 0.18$ (0), $x = 0.19$ (0, 50, 100, 200, 500 Oe), $x = 0.20$ (0), $x = 0.21$ (0, 100, 200, 500), $x = 0.23$ (0, 30, 70, 200, 500, 1000 Oe), $x = 0.25$ (0, 50, 100, 500, 1000 Oe) and $x = 0.27$ (0, 20, 50, 100, 200, 350, 500, 1000 Oe), respectively.

These equations form the basis of estimates of the ordering temperature T_C and the critical exponents δ, γ and β through the detailed, self-consistent analysis of magnetic isotherms [46–50].

Continuous/second-order PM–FM transitions can also be characterized using the behaviour of the ac susceptibility in various superimposed static magnetic fields (H_a), as the application of such fields enables a series of critical susceptibility maxima to be resolved, the temperature (T_m) of which increases while the amplitude ($\chi(H_a, T_m)$) decreases as H_a is increased. As discussed in detail previously, the field dependence of these latter peaks can also derived from equation (3) which, assuming the validity of the Widom equality ($\gamma + \beta = \beta\delta$) [18, 45–47, 51], yields

$$\chi(h,t) = \frac{\partial m}{\partial h} = |t|^{-\gamma} G_{\pm}\left(\frac{h}{|t|^{\gamma+\beta}}\right) = h^{1/\delta-1} Y_{\pm}\left(\frac{h}{|t|^{\gamma+\beta}}\right) \tag{7}$$

$G_{\pm}(x)$ being the derivative of $F_{\pm}(x)$ w.r.t. its argument. Correspondingly, standard scaling theory predicts that the locus and amplitude of these peaks are governed by a set of power-law predictions, discussed previously in detail [16, 18, 51], namely:

$$\chi(H_i, t_m) \propto H_i^{1/\delta-1} \tag{8}$$

$$t_m = (T_m - T_C)/T_C \propto H_i^{1/(\gamma+\beta)} \tag{9}$$

$$\chi_m \propto t_m^{-\gamma}. \tag{10}$$

Here the reduced peak temperature $t_m = (T_m - T_C)/T_C$ determines the location of the 'cross-over' line—the locus of the susceptibility maxima—above which the response is thermally dominated, as opposed to being field-dominated below it [16, 18, 45–48].

The zero-field ac susceptibilities (reproduced in figure 2(a)) enable two important estimates to be made. First, the maximum susceptibility, often referred to as the Hopkinson/principal maximum [45–48], provides an experimental determination of the demagnetization factor, $N_D = 1/\chi_{max}$, used below to make demagnetization corrections. Second, the inflection points in ac susceptibilities yield preliminary estimates for ordering temperatures, T_C. These estimates enable subsequent magnetization/susceptibility measurements to be focused around the critical region.

3.2.2. $x = 0.18$ and 0.20

Magnetization. As these two single crystals display no GP-like features, their behaviour is the simplest to analyse. Arrott plots [52] ($M^2 \sim H_i/M$, but not reproduced here) for the corresponding data display a positive slope (i.e. no term of the form $-a(T)M^4$ in the free energy [44]) throughout the transition region, confirming the continuous/second-order nature of the PM–FM transition. Based on the modified Arrott–Noakes equation of state [53], these data were subsequently plotted using a range of model exponents, which iterate towards values consistent with Heisenberg model predictions ($\gamma = 1.387$, $\beta = 0.365$ (and $\delta = 4.783$)) [19], namely $(H_i/M)^{1/1.387}$ versus $M^{1/0.365}$, as shown in figure 4(a) for the $x = 0.18$ sample (the corresponding data for $x = 0.20$ being essentially identical). Self-consistency is ensured by taking the intercepts from this latter figure (that on the vertical axis giving the spontaneous magnetization, M_S, and the horizontal axis, the inverse initial susceptibility, $1/\chi_i$) and testing them against the corresponding power-law predictions, equations (5) and (6), as shown in figures 4(b) and (c); the slopes of the inserts in these figures yield marginally refined exponent estimates. This process is then iterated until minimal changes in exponent values result [18, 45–48]. The critical isotherm yields a value for T_C, with the associated magnetization (figure 4(b)) being tested against the predictions of equation (4), as shown in the insert in this latter figure. This procedure yields values of $T_C = 170 \pm 1$ K, $\gamma = 1.36 \pm 0.01$, $\beta = 0.36 \pm 0.01$ and $\delta = 4.77 \pm 0.01$ (3 kOe $< H <$ 90 kOe) for $x = 0.18$ (with $T_C = 179 \pm 1$ K, $\gamma = 1.34 \pm 0.01$, $\beta = 0.37 \pm 0.01$ and $\delta = 4.79 \pm 0.01$ (4 kOe $< H <$ 90 kOe) from the corresponding data at $x = 0.20$). Both sets of estimates agree with Heisenberg model predictions within experimental uncertainty, and satisfy the Widom equality $\gamma = \beta(\delta - 1)$ [44]. The δ estimates, incidentally, confirms—albeit indirectly—the absence of GP-like behaviour, as the latter is frequently characterized by large δ values [15, 16], an issue addressed in more detail below.

AC susceptibility. The evolution of the ac susceptibility peak structure with field and temperature, typified by the data in figure 5(a) for the $x = 0.20$ single crystal, provides confirmatory evidence of the continuous nature of the accompanying phase transition, and provides independent estimates of both the critical exponents and ordering temperatures. Figures 5(b)–(e) summarize the analysis of such ac susceptibility peak data, in terms of scaling law predictions, equations (8)–(10). Figure 5(b) reproduces a plot of the critical peak amplitudes χ_m (corrected for background and demagnetizing effects)—taken from the equivalent of figure 5(a) for $x = 0.20$—against the internal field H_i on a double-logarithmic scale; this not only confirms the power-law dependence of equation (8), but its slope also yields an estimate of $\delta = 4.78 \pm 0.01$ for $x = 0.20$ (and from the equivalent data at $x = 0.18$, $\delta = 4.78 \pm 0.01$). These estimates are clearly independent of any choice for T_C, indicating that ac susceptibility measurements provide a distinct advantage over conventional magnetization-based approaches, for which the determination of the ordering temperature is a prerequisite prior to extracting estimates for δ from data taken by attempting to stabilize along the critical isotherm. The remaining exponent values, however, require a choice for T_C to be made; this is done—based on equation (9)—by plotting the measured peak temperatures, T_m, against the internal field $H_i^{0.57}$ (i.e. assuming the applicability of Heisenberg model exponents, namely $(\gamma + \beta)^{-1} = 0.57$ [19, 45–47], as suggested by the δ estimate, above), and extrapolating to $H_i = 0$, as shown in figure 5(c). This yields $T_C = 179 \pm 1$ K for the $x = 0.20$ sample (with $T_C = 170 \pm 1$ K found similarly for $x = 0.18$). This initial T_C estimate is then used to construct the double-logarithmic plots of the reduced temperatures t_m against the internal fields H_i (equation (9))

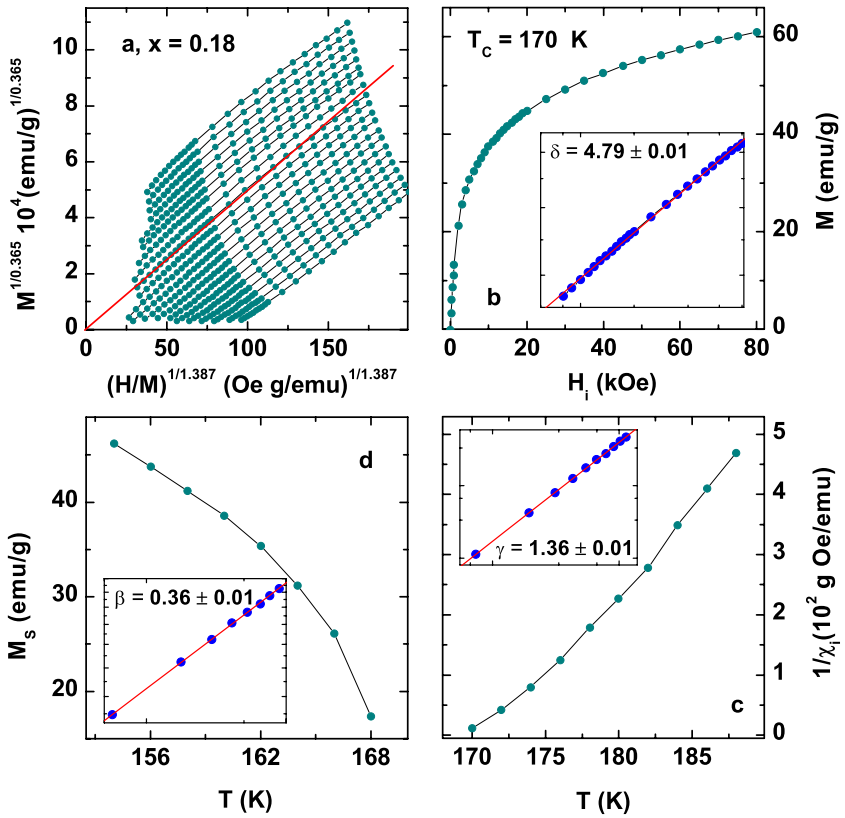

Figure 4. For $x = 0.18$. (a) Selected magnetic isotherms replotted in the form $(H_i/M)^{1/1.387}$ versus $M^{1/0.365}$ (from 150 K (upper) to 190 K (bottom) in 2 K steps); the critical isotherm passing through the origin yields $T_C = 170$ K. (b) Plot of M versus H_i along the critical isotherm; inset is the corresponding double-logarithmic plot, the slope of the line drawn yielding $\delta = 4.79 \pm 0.01$ for 4 kOe $< H <$ 90 kOe. (c) The inverse initial susceptibility, $1/\chi_i$, plotted against temperature T: inset; $1/\chi_i$ versus reduced temperature t on a double-logarithmic scale, yielding $\gamma = 1.36 \pm 0.01$. (d) The spontaneous magnetization $M_S(T)$ plotted against T: inset; M_S versus t on a double-logarithmic scale, yielding $\beta = 0.36 \pm 0.01$.

shown in figure 5(d), and of the peak amplitudes χ_m against the reduced temperatures t_m (equation (10)), figure 5(e). The slopes of such plots yield initial estimates for $(\gamma + \beta)^{-1}$ and γ^{-1}, respectively. Subsequently, this process is iterated, accompanied by small adjustments in T_C, until self-consistency is achieved. Thus values of $\beta = 0.38 \pm 0.01$, $\gamma = 1.38 \pm 0.01$ and $T_C = 179 \pm 1$ K were obtained at $x = 0.20$ (while using the same approach at $x = 0.18$ yields $\beta = 0.37 \pm 0.01$, $\gamma = 1.38 \pm 0.01$ and $T_C = 170 \pm 1$ K), both parameter estimates being in excellent agreement with the analysis of the magnetization data.

A final test of these exponent value estimates for—and hence the applicability of 3D Heisenberg model exponents to—these samples is provided in figures 6, using the magnetic isotherms reproduced in figure 4(a) and ac susceptibility data shown in figure 5(a) (and their equivalents for $x = 0.20$). The magnetization scaling using the above listed T_C's and exponent estimates, based on equation (3), is carried out in figure 6(a); both demonstrates good data collapse. Susceptibility scaling is based on equation (7); specifically, such data, when normalized to its peak value $(\chi(h, T_m))$, should collapse onto a universal curve when plotted against the argument $(h/t_m^{(\gamma+\beta)})$ of the scaling function (actually, its inverse, $t_m/h^{1/(\gamma+\beta)}$ to preserve the peak structure [18, 45–47]), as confirmed in figure 6(b). In summary, the above analysis provides consistent estimates for the ordering temperatures T_C and demonstrates convincingly that the exponent estimates agree, within experimental uncertainty, with those of the 3D Heisenberg model and thus satisfy the Widom equality.

3.2.3. $x = 0.19$. As can be seen from figure 3, this single crystal displays features characteristic of GP-like behaviour; what is also evident from this figure is that such features are rapidly suppressed by an applied field. Such a result is expected since a uniform applied field is the conjugate field for collinear ferromagnetism, enhancing the latter at the expense of its non-uniform Griffiths counterpart [36, 37, 48, 51]; what is not understood at present are the parameters that determine the *rate* at which such a suppression occurs with applied field [36]. At $x = 0.19$ this suppression is rapid, as the following demonstrates. Arrott plots again confirm the continuous nature of the PM–FM transition. Following the procedure outlined earlier, these data could be linearized initially using the same exponent values as those deduced above, namely $(H_i/M)^{1/1.387}$ versus $M^{1/0.365}$, and hence are not reproduced here; neither are plots based on the analysis outlined above as it yielded very similar exponent estimates of $\delta = 4.78 \pm 0.01$ (3 kOe $< H <$ 90 kOe), $\gamma = 1.36 \pm 0.01$ and $\beta = 0.37 \pm 0.01$ with $T_C = 172 \pm 1$ K. As mentioned earlier, GP-like features are often accompanied by large δ

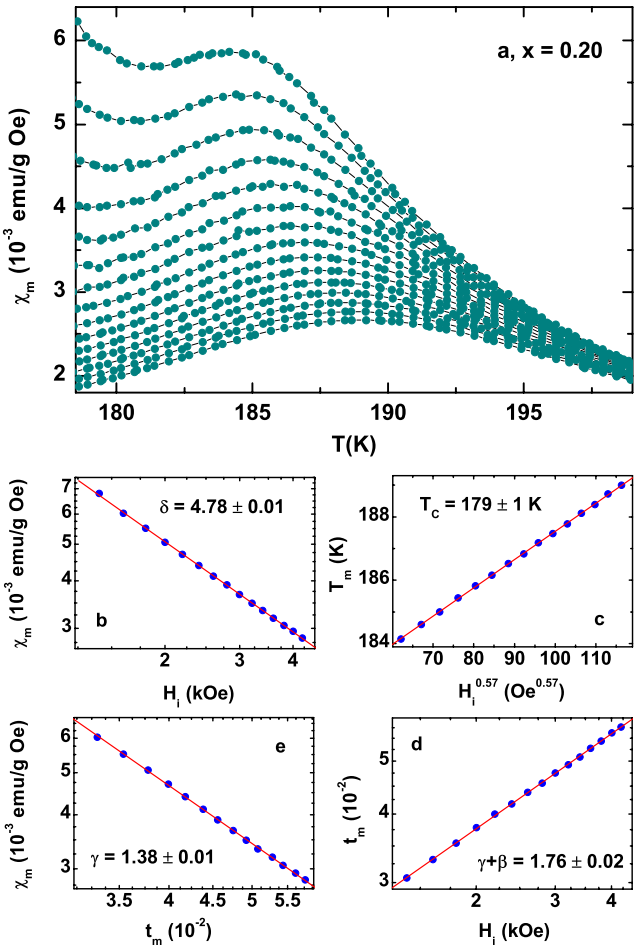

Figure 5. For $x = 0.20$. (a) $\chi(H, T)$ (corrected for background and demagnetizing effects) measured on warming following ZFC in fixed static fields of 1.4 kOe (top) to 4.2 kOe (bottom) in 200 Oe steps. Double-logarithmic plots testing the power-law predictions of equations (8)–(10): (b) the peak susceptibilities χ_m versus the internal field H_i, the slope yielding $\delta = 4.78 \pm 0.01$: (c) estimate of the critical temperature used above from extrapolation of the susceptibility peak temperatures T_m against $H_i^{0.57}$ yielding $T_C = 179 \pm 1$ K: (d) reduced peak temperature t_m against H_i, yielding $\gamma + \beta = 1.76 \pm 0.02$; (e) χ_m against t_m yielding $\gamma = 1.38 \pm 0.01$ and hence $\beta = 0.38 \pm 0.01$.

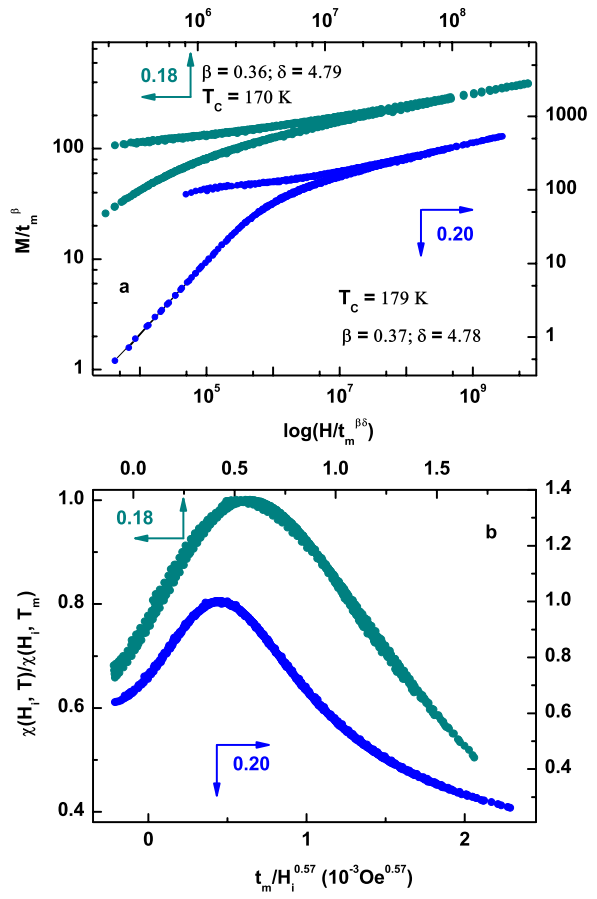

Figure 6. (a) Conventional magnetization scaling plot (equation (4)) on a double-logarithmic scale using the critical exponents and T_C listed above for $x = 0.18$ and 0.20. The upper branch corresponds to data below T_C and the lower branch to data above T_C. (b) Susceptibility scaling plots for the isokaps for $x = 0.18$ and 0.20.

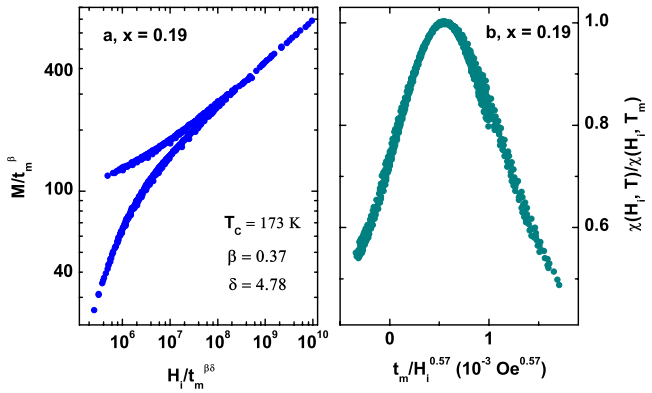

Figure 7. For $x = 0.19$. Scaling plots for (a) the magnetization and (b) the susceptibility.

values [15, 16]; such behaviour is not, however, observed in this $x = 0.19$ sample, first, because GP-like features are rapidly suppressed by field and, second, because *low*-field data (those typically below 0.5–1 kOe, where such features *are* present) are seldom included in scaling analyses to avoid both technical contributions and the relatively large uncertainties associated with demagnetization corrections prevalent in that field range [48, 49]. A similar situation occurs in the analysis of ac susceptibility data on this single crystal. Here a critical peak structure similar to that shown in figure 4(a) emerges, but as fields in excess of 1.5 kOe have to be applied to first resolve this structure, such fields completely suppress GP-like characteristics in *this* sample. The analysis of these ac susceptibility data in the manner outline earlier yields $\delta = 4.79 \pm 0.02$, $\beta = 0.37 \pm 0.01$ and $\gamma = 1.38 \pm 0.01$, with $T_C = 172 \pm 1$ K, in close agreement with the analysis of magnetization data and, again, with model predictions for the 3D Heisenberg model. These data are thus presented in summary form only in figure 7, where magnetization and ac susceptibility data collapse can be seen to be accomplished using the parameters listed above.

This $x = 0.19$ Ca-substituted single crystal thus displays properties very similar to single-crystal $La_{0.73}Ba_{0.27}MnO_3$ [48]; both show signatures of GP-like behaviour but with an

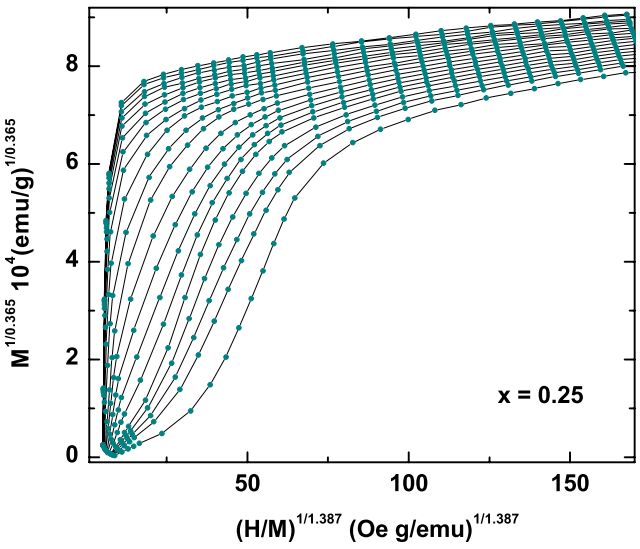

Figure 8. For $x = 0.25$. Plot of $(H_i/M)^{1/1.387}$ versus $M^{1/0.365}$ for the selected magnetic isotherms from 180 to 200 K in 1 K steps.

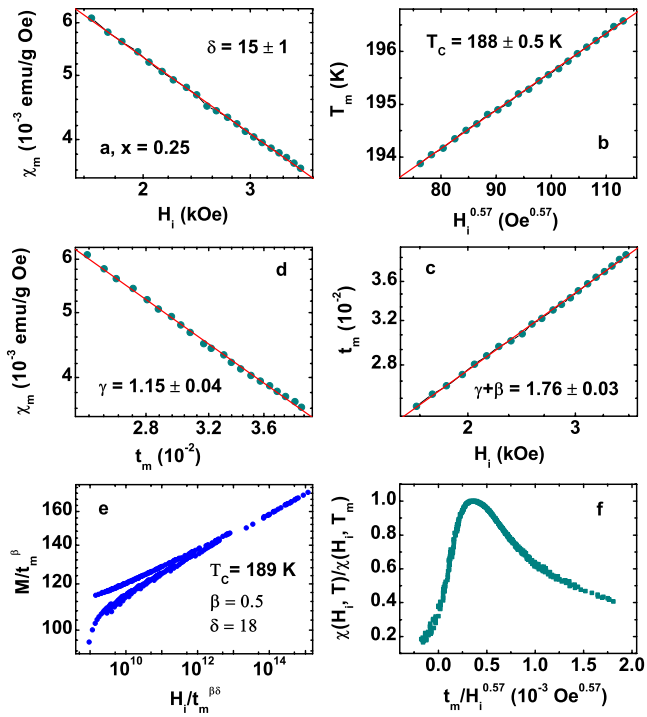

Figure 9. For $x = 0.25$. Double-logarithmic plots testing the power-law prediction of equations (8)–(10), yielding $\delta = 15 \pm 1$, $\gamma = 1.15 \pm 0.04$, $\beta = 0.51 \pm 0.02$ and $T_C = 188 \pm 1$ K. Magnetization (e) and susceptibility (f) scaling plots.

insulating ground state, and δ values close to those of the Heisenberg model due to the rapid field-induced suppression of GP-like features. This point is discussed in more detail below. Given the near Heisenberg model behaviour of the three single crystals with $x = 0.18$, 0.19 and 0.20, their critical amplitudes, E in equation (4), were estimated from power-law plots and listed in table 1. Since this table contains a comprehensive survey of parameters obtained by fitting magnetization, susceptibility and transport data, further discussion of its content is deferred at this point.

3.2.4. $x = 0.21$, 0.23 and 0.25. As might be anticipated, the presence of GP-like characteristics complicates the analysis of the magnetic critical behaviour of these three single crystals in varying degrees. While Arrott plots exhibit positive slopes throughout the transition region, confirming the occurrence of a continuous PM–FM transition, modified Arrott–Noakes plots, using a range of models, fail to linearize the magnetization-field data at these compositions. Figure 8 illustrates this point for the $x = 0.25$ single crystal using Heisenberg exponent values (confirming recent conclusions for the $x = 0.21$ sample [16]). Such a result has been linked previously with the presence of GP-like behaviour [15, 16]. As a consequence critical analysis, based on the temperature- and field-dependent magnetization of the type performed above for $0.18 \leqslant x \leqslant 0.20$, is precluded at these higher substitution levels.

The field-dependent ac susceptibility, in contrast, does not suffer from this limitation; in all three of these samples a peak structure similar to that shown in figure 5(a) emerges and can be analysed in the manner described above. The emergence of this peak structure, incidentally, supports the conclusion that the transition is continuous. Figure 9(a) provides an estimate for the exponent $\delta = 15 \pm 1$ for $x = 0.25$ directly, i.e. prior to the identification of T_C, as described above; similarly $\delta = 19 \pm 1$ ($x = 0.21$) and $\delta = 5.5 \pm 0.3$ ($x = 0.23$). Such estimates far exceed that for the 3D Heisenberg model, at least for $x = 0.21$ and 0.25, a result typically accompanying GP-like characteristics in some doped CMR perovskites [15, 16]: at $x = 0.23$ the δ estimates marginally exceed the model values—as in $La_{0.7}Ba_{0.3}MnO_3$, which also exhibits GP-like features [37]—a issue addressed in more detail later. Furthermore, since estimates for the critical amplitude E (equation (4)) depend crucially on the value for δ [48], no such estimates are listed for these single crystals. To extract other exponent estimates, a value for T_C must be established *quantitatively*. As reported recently for the $x = 0.21$ single crystal [16], despite the non-standard values for δ, plots of T_m against the internal field $H_i^{1/(\gamma+\beta)}$ using Heisenberg model exponents provides an excellent representation of the data between $x = 0.21$ and 0.25. This is a fortuitous result, but one enabling a quantitative estimate for T_C to be made, as confirmed in figure 9(b) for $x = 0.25$ (with equivalent results at $x = 0.21$ and 0.23). Nevertheless, while the *sum* of these two exponents combine to the Heisenberg model value, the remaining two scaling plots—figures 9(c) and (d)—indicate that *individual* exponent values differ from model predictions. The results emerging from these latter two figures yield: $\beta = 0.51 \pm 0.02$, $\gamma = 1.15 \pm 0.04$, with $T_C = 188 \pm 1$ K for this $x = 0.25$ single crystal (correspondingly $\beta = 0.09 \pm 0.02$, $\gamma = 1.65 \pm 0.01$, with $T_C = 182 \pm 1$ K for $x = 0.21$ (in excellent agreement with a recently reported result [16]), while $\beta = 0.43 \pm 0.02$, $\gamma = 1.35 \pm 0.01$, with $T_C = 185 \pm 1$ K for $x = 0.23$).These non-standard estimates satisfy the Widom equality, within experimental uncertainty, for the $x = 0.21$ single crystal, but not its $x = 0.23$ and 0.25

counterparts; nevertheless, they also provide data collapse for both ac susceptibility *and* magnetization data for all of these samples, as figures 9(e) and (f) confirm.

3.2.5. $x = 0.27$. As aspects of the unusual magnetic response at this composition have been reported previously [54], here we focus on issues related to the continued presence of GP-like features at this composition (figure 3). Briefly, therefore, figure 10(a) summarizes magnetization data in fields up to 15 kOe in the vicinity of 240 K, which confirm both the metamagnetic/'S'-like character of the response near this temperature and the occurrence of weak hysteresis. Both features are consistent with the presence of a discontinuous/first-order PM–FM transition, a conclusion supported by Arrott plots for the corresponding data, figure 10(b), which can be seen to exhibit negative slopes over part of the (H–T) plane encompassing these data. Nevertheless, field-dependent ac susceptibilities display a peak structure reminiscent of figure 4(a), features normally associated with continuous/second-order transitions. As reported earlier [54], the usual tests of the evolution of these 'pseudo-critical' peaks with field and temperature fail to confirm power-law behaviour, they display continuous curvature, precluding estimates for critical exponents. Specifically, that Heisenberg model exponents do not describe these data is confirmed by the corresponding modified Arrott–Noakes plots, figure 10(c).

It is important to (i) reiterate that the response summarized above is fundamentally different from cross-over effects accompanying a sequential second-order to first-order transition as the temperature is lowered towards T_C. In such a situation the first-order transition line would lie *below* that for the continuous transition; here it does not. A plot of the peak temperatures in the ac susceptibility against field combined with those for the metamagnetic fields (the inflection points in figure 10(a)—a signature of the first-order transition line [50]) against temperature are contiguous. This plot exhibits curvature at low field [54], but nevertheless admits a reasonable extrapolation yielding $T_C = 228 \pm 3$ K (close to the inflection point in the zero-field ac susceptibility, figure 2(g)). This behaviour supports the assertion that in this $x = 0.27$ single crystal the characteristics of both first-order and second-order transitions are essentially *coincident*. And (ii) to note that above this transition line the present data demonstrate the continuing presence of GP-like behaviour, although measurements at still higher Ca substitution (approaching optimal doping, $x = 0.33$) indicate the termination of such behaviour with the emergence of a first-order transition alone [50].

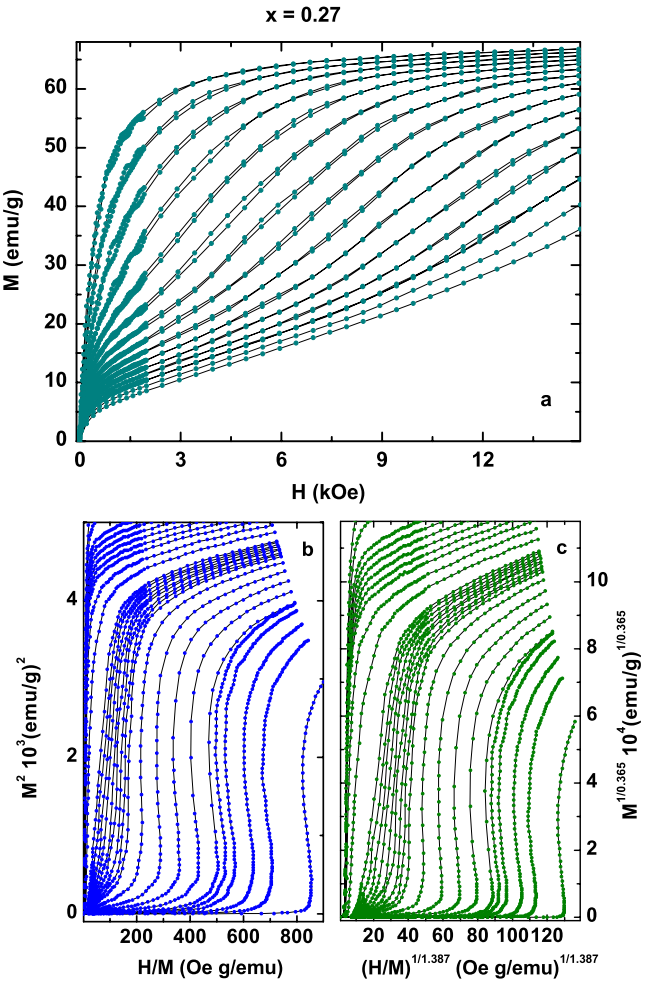

Figure 10. (a) Selected magnetic isotherms measured from 234 to 238 K in 1 K steps for fields up to 15 kOe. The existence of hysteresis demonstrates that the transition is first order. (b) Arrott plots—H_i/M versus M^2—for magnetic isotherms from 210 to 220 K in 5 K steps, and from 222 to 260 K in 2 K steps. (c) Plot of $(H_i/M)^{1/1.387}$ versus $M^{1/0.365}$ for data in (b).

3.3. Transport behaviour

Prior to discussing the implications of the magnetic data, a detailed examination of the transport properties is appropriate. This is accomplished via quantitative fits to these data of the various model predictions. In particular, the temperature dependence of the resistivity in the *high* temperature PM insulating phase ($d\rho/dT < 0$) above T_C in many doped Mn perovskites has been fitted to a modified Arrhenius law of the form [55, 56]

$$\rho(T) = \rho_0 T^{\alpha} \exp(E_a/k_B T). \tag{11}$$

Here E_a is related to the polaron formation energy, while the exponent α can assume values of 0, 1 or 3/2, depending on the physical model invoked—0 for simple thermally activated hopping, 1 for adiabatic and 3/2 for non-adiabatic small polaron hopping. The prefactor ρ_0 includes a carrier density factor $4x(1-x)/V$, in which the term $x(1-x)$ accounts for site occupation effects [55, 56], with V being the double-cell volume. For the present single crystals, the non-adiabatic small polaron hopping version of equation (11) ($\alpha = 3/2$) provides the most convincing fit to available data in the high temperature regime (as judged by the associated standard deviation); this fit is also clearly superior to that afforded by variable range hopping, despite the application of the latter to this system at lower doping levels [57]. Representative fits to zero-field data are shown in figures 11(a) and (b) (for

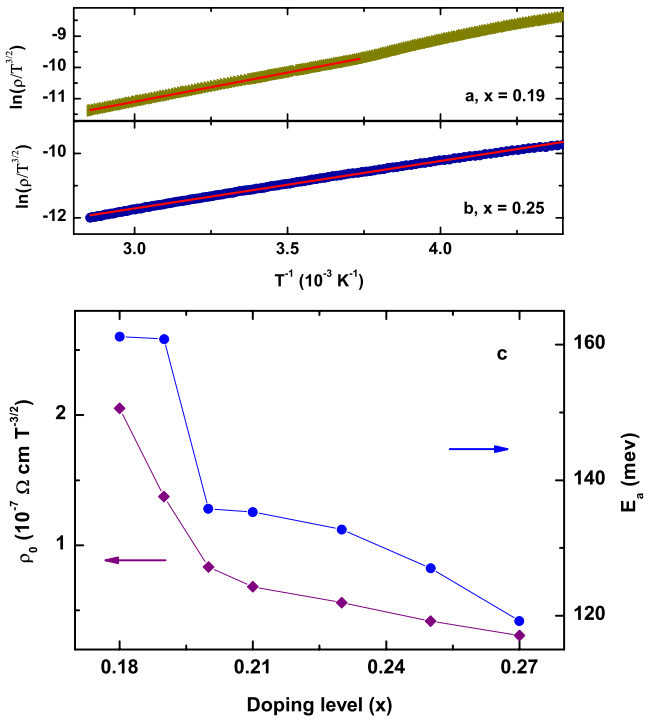

Figure 11. Zero-field resistivity reproduced in the linearized form of equation (11), namely $\ln(\rho/T^{3/2})$ versus T^{-1}. Figures 11 (a) and (b) correspond to $x = 0.19$ and $x = 0.25$, respectively. The linear fits yield the corresponding excitation energy E_a and the prefactor ρ_0, both of which are plotted as a function of doping level x in (c).

single crystals below ($x = 0.19$) and above ($x = 0.25$) the M–I threshold) using the linearized form of equation (11), namely $\ln(\rho(T)/T^{3/2})$ versus T^{-1}, yielding estimates for E_a and ρ_0. These E_a estimates (listed in table 1 for all samples) fall within the general range reported for a variety of manganites [30, 31, 55, 56][3]. Figure 11(c) reproduce these E_a and ρ_0 estimates as a function of doping level x. Here a sharp decrease in the polaron formation energy, E_a, is clearly evident on crossing the compositionally modulated I–M boundary; as such, it appears as a precursor effect appearing in the PM regime prior to the establishment of insulating ground state properties below $x = 0.20$. In general terms, the emergence of such a ground state has been linked with local structural changes, namely the structure that controls carrier (e_g) (de)localization [23–29]. Quantitatively it has been characterized by the absence/presence of the so-called Jahn–Teller (JT)-long-bond accompanying an orbitally ordered (OO) (insulating) to orbitally disordered (OO*) (metallic) transition [23–27]. The present results suggest that the latter influences the energy controlling polaron formation, extending the correlation between JT distortions and both the transport and magnetic response across this compositionally modulated phase boundary established previously [23–26], While the prefactor ρ_0 also decreases with increasing doping level, it does so less abruptly, providing a weaker indication from the PM regime regarding the disappearance of metallicity.

[3] This observation conforms with the results of small-angle neutron scattering (De Teresa *et al* [58]) and recent high temperature inverse ac susceptibility and transport data [17]; Souza *et al* [58].

As for the magnetoresistance, in the $x = 0.18$ single crystal, apart from the principal maximum near T_C, additional transitions are evident via two secondary peaks in $\Delta\rho = [\rho(0) - \rho(H)]/\rho(H)$, shown in the inset in figure 1(a). These reflect a low temperature, structurally driven transition near $T_B \approx 70$ K accompanying a decrease in orthorhombicity, and a higher temperature Jahn–Teller transition around $T_{JT} \approx 270$ K (corresponding to a pseudo-cubic to orthorhombic structural change [28]); the latter is also evident in the inverse ac susceptibility. Such additional features are not evident at higher doping levels, $0.19 \leqslant x \leqslant 0.27$, where the magnetoresistance/CMR, $\Delta\rho$, displays no systematic trend with doping level.

3.4. Evolution of ferromagnetism

The present data provide a careful delineation of the compositionally driven M–I boundary as lying between 19 and 20% Ca substitution in this series of single crystals, thereby supplying incontrovertible evidence that the emergence of metallicity and ferromagnetism are *not* coincidental in $La_{1-x}Ca_xMnO_3$. The latter emerges prior to the former, prompting the question of what are the principal mechanisms underlying ferromagnetism in this composition range? As suggested recently [59], whereas FM-DE, stabilized by hole delocalization, dominates in the metallic regime immediately above the compositionally controlled M–I boundary, the relevant interaction below this boundary is *ferromagnetic* super-exchange (SE). As briefly outlined by Jiang *et al* [59], this proposal is based on the evolution of SE with composition, x. The SE-dominated, undoped parent $LaMnO_3$, exhibits in-plane FM interactions (the corresponding exchange coupling $J_{ab} > 0$), whereas intra-/out-of-plane interactions are AFM ($J_c < 0$), leading to a quite different magnetic ground state from that prevalent at $x = 0.18$ and beyond. In the undoped parent the magnetic structure is induced/stabilized by the OO [6] (viewed alternatively, it is a consequence of the semi-empirical Kanamori–Goodenough–Anderson (KGA) rules in which the sign of SE coupling is modulated by the Mn–O–Mn bond angles and bond lengths). Neutron scattering measurements [27] have provided evidence at the microscopic level regarding the evolution of SE coupling with doping level in this system, showing that while the magnitude of FM–SE in-plane coupling, $J_{ab}(x)$, increase monotonically with increasing doping level in the region of interest here, the evolution of the c-axis coupling, $J_c(x)$, is more complex. Specifically, $J_c(x < 0.125) < 0$ (as in the undoped parent) $J_c(x = 0.125) = 0$, while $J_c(0.125 < x < 0.22) > 0$, increasing roughly linearly with doping for $x > 0.125$. Thus *both* $J_{ab}(x)$ and $J_c(x)$ are positive/FM across the compositionally modulated M–I boundary and this is where ferromagnetism first emerges in $La_{1-x}Ca_xMnO_3$.

Two issues emerge immediately: the first concerns the universality class for the PM–FM transition between $x = 0.18$ and 0.20, which the above analysis demonstrates conclusively is that of the nearest-neighbour 3D Heisenberg model: the second relates to the critical amplitude, E of equation (4). The latter shows little variation across the compositionally modulated M–I transition between $x = 0.18$ and 0.20

(table 1). To address the second issue first, since this critical amplitude is a direct measure of the *number* of spins involved in the transition [60], then once the ferromagnetism is established (more appropriately in the present context, an infinite/percolating FM 'backbone'), minor increases in the number of spins coupled to this backbone accompany further, additional increases in hole doping in this regime. Thus E should display little variation with x across the M–I threshold, as is observed. It is the dominant *mechanism* that changes from insulating to metallic phase. To estimate a critical amplitude such as E, the scaling behaviour of the transition in question must fall into a specific universality class (i.e. exhibit a specific power-law dependence)—here that of the isotropic 3D Heisenberg model. Comparisons with samples exhibiting GP-like characteristics, for the power law along the critical isotherm is radically different, are thus inappropriate. For the universality class, Monte Carlo simulations for the DE model [20, 21] *without* anisotropy do indeed predict that it should fall into that for the 3D Heisenberg system, as the analysis of the above data confirm. However, DE coupling in systems with a *non-cubic* structure should acquire some anisotropy/directional dependence. That this is not observed in the current experiments likely reflects the scale of such anisotropy compared with thermal energies, $k_B T_C$, in the vicinity of the ordering temperature. Similar comments apply in insulating specimens where FM–SE is the principal interaction mechanism; here neutron data indicate that $J_{ab}(x)$ and $J_c(x)$ differ by only some 0.5 meV near $x = 0.19$ [27]. The current data indicate that exponent values characterizing this latter interaction also lie in the universality class of the 3D Heisenberg model. While we are not aware of any theoretical prediction that confirms this result, data on the magnetoresistive pyrochlore $Tl_2Mn_2O_7$ in which FM–SE dominates confirm such an assignment [47]. Indirect evidence supporting the above assertion is also provided by the use of the same model exponents in reproducing the dispersion relation for magnetic excitations measured at $x < x_c$ [27] in $La_{1-x}Ca_xMnO_3$.

Such similarities notwithstanding, the data presented above indicate that the percolation threshold for these two interaction mechanisms are unequivocally different in $La_{1-x}Ca_xMnO_3$ [61], despite the near-neighbour interaction range frequently assumed to characterize them. The relative interaction *strengths* must, however, be comparable. The present data—acquired from samples with more closely spaced compositions than those reported earlier [59]—indicate that dT_C/dx is unchanged (within experimental uncertainty) for compositions spanning the M–I boundary ($dT_C/dx = 3 \pm 1.4$ K for both the two insulating and the two metallic samples immediately adjacent to this boundary, with the actual 'best fit' T_Cs yielding identical values for this slope across the boundary in question).

Support for the comparability of these two interaction strengths is also provided by estimates of the acoustic spin-wave stiffness, D [12], obtained from estimates made for the spontaneous magnetization ($M_S(T)$) using extrapolations based on a modified Arrott–Noakes equation of state [52, 53]. These estimates are reproduced in figure 12 and have been

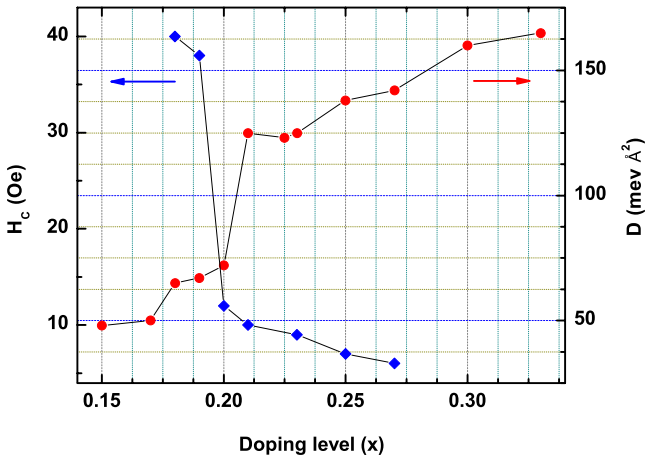

Figure 12. Coercivity H_C at 10 K acquired from both (magnetization) hysteresis and susceptibility butterfly loops on the left side. Spin-wave stiffness D found from the low temperature spontaneous magnetization M_S on the right side. Data for $x = 0.15$, 0.17, 0.225 and 0.33, are taken from [28] and [29].

fitted to the Bloch $T^{3/2}$ law [62, 63], a temperature dependence originating from the assumption of gapless acoustic spin-wave excitations described in the usual notation by the dispersion relation $\hbar\omega_{ac} = Dq^2$ leading to the following well-known expression for the temperature dependence of the spontaneous magnetization, $M_S(T)$, [62–64], namely

$$\frac{M_s(T)}{M_S(0)} = 1 - \frac{1}{NS}\left(\frac{k_B T}{4\pi D(T)}\right)^{3/2} \cdot \xi\left(\frac{3}{2}\right) \qquad (12)$$

$\xi(3/2)$ being the Riemann zeta function. A least-squares fit of these data to equation (12) yield D and the zero temperature spontaneous magnetizations, M_S (0) (table 1). The former are plotted as a function of doping level in figure 12, from which it can be seen that D varies *smoothly* across the compositional M–I boundary. This behaviour of D thus correlates with the critical behaviour, with lower D values (~65 meV Å^2) appearing in both insulating and metallic samples exhibiting Heisenberg model exponent values. Quantitatively, $D = 2JSa^2$ for interacting near-neighbour spins (S) with separation a (at least in cubic symmetry), J being the associated SE or DE interaction strength. Comparable values for D on either side of the M–I boundary thus imply comparable magnitudes for the prevailing dominant interactions. Figure 12 also shows that D increases sharply deeper into the metallic phase, but only at compositions at which GP-like features emerge [16]. This result supports the earlier suggestion that differences in behaviour accompanying the latter in metallic samples are not simply manifested in a modified critical response near T_C, but extend throughout the magnetically ordered regime. Furthermore, these values for D estimated for the insulating regime of $La_{1-x}Ca_xMnO_3$ agree with those reported in *ferromagnetic* $Pr_{1-x}Ca_xMnO_3$ ($x = 0.27$, 0.29) where the ground state is not only insulating, but the critical exponents also fall into the universality class of the 3D Heisenberg model [18]. It is clear that the insulating character of this latter system precludes DE as a dominant coupling mechanism [18],

supporting the assertion made above regarding the universality class appropriate for $La_{1-x}Ca_xMnO_3$ in its insulating regime.

Finally, the coercivity, H_C, estimated from magnetization isotherms and susceptibility butterfly loops at 10 K, increases sharply in those single crystals with an *insulating* ground state. As discussed above, FM–SE emerges just below the (insulating) OO to (metallic) OO* boundary, thus ferromagnetism in this region is stabilized by orbital ordering [59, 65]. As the coercivity is determined from the response of the magnetization/spin to applied fields, then the onset of orbital order would be expected to lead to an increase in H_C. The presence of spin–orbit coupling combined with the specific orientational structure reflecting orbital ordering characteristics is equivalent to anisotropy, thus impeding any magnetization/spin rotation, leading to increased coercivity, as indeed is observed (figure 12) (domain wall effects notwithstanding).

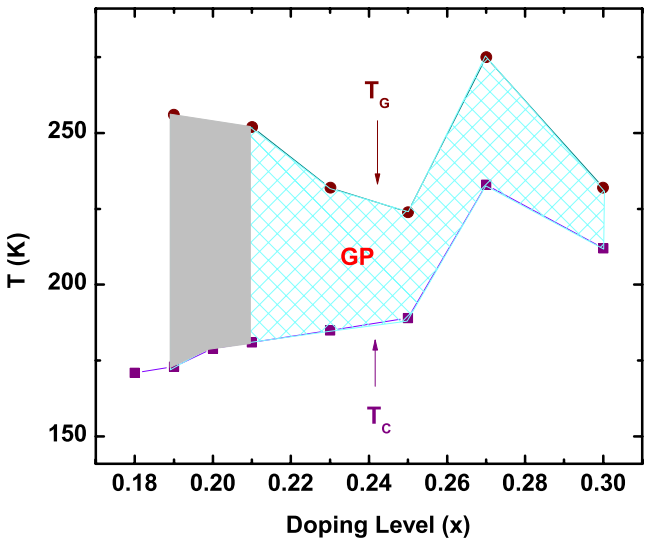

Figure 13. Phase diagram for $La_{1-x}Ca_xMnO_3$ ($0.18 \leqslant x \leqslant 0.33$).

4. Summary and conclusion

Temperature-dependent (magneto)transport measurements demonstrate that the compositionally modulated M–I transition lies between $0.19 \leqslant x_c \leqslant 0.20$ for the single-crystal $La_{1-x}Ca_xMnO_3$ series studied. The evolution of this system from the OO insulating toward the OO* metallic state accompanying increasing levels of Ca substitution underlies the emergence of FM–SE (as seen in neutron scattering data). This latter interaction, it is argued, dominates the magnetic ordering process in the insulating phase immediately adjacent to the compositionally modulated M–I transition; on crossing the latter, DE becomes the dominant interaction as metallicity emerges. The compositional variation of both the acoustic spin-wave stiffness (D) and the coercive field (H_C) support this assertion.

The universality class of the transition accompanying both FM–SE and DE-dominated ordering is shown to be that of the isotropic, near-neighbour 3D Heisenberg model; nevertheless, the percolation thresholds for these two interactions are manifestly different. Evidence of GP-like features appear in the low-field ac susceptibility for samples exhibiting both the insulating and metallic ground states, although such features are rapidly suppressed by small applied fields (the fields conjugate to *uniform* ferromagnetism) for $x < 0.21$, leading to a Heisenberg model-like critical response. Combined with the magnetotransport measurements, the latter not only confirms that GP-like features are *not* a prerequisite for CMR [16], but also impose the important caveat that GP-like features do not *guarantee* the appearance of CMR.

With the adoption of a working definition of the Griffiths temperature, T_G, as the temperature at which a marked onset depression in the inverse zero-field ac susceptibility first occurs [41] (marked by vertical arrows in figure 3), a phase diagram for $La_{1-x}Ca_xMnO_3$ ($x < 0.33$) can be constructed, figure 13. This affords comparisons with those reported previously for $La_{1-x}Sr_xMnO_3$ ($0.075 \leqslant x \leqslant 0.175$) [34] and $La_{1-x}Ba_xMnO_3$ ($0.10 \leqslant x \leqslant 0.33$) [37]. In the present system, the GP-like regime terminates in close proximity to the M–I boundary, but, as mentioned above, the emergence of such features near this boundary may be particularly sensitive to various aspects of the underlying 'disorder', possibly including the stoichiometry (the latter may also play a role in the variation evident in T_G and T_C estimates in this Ca-doped system, mentioned earlier). The termination of this region is consequently marked as hatched, the latter also delineating—likely non-coincidentally—the M–I boundary at $0.19 \leqslant x_c \leqslant 0.20$ in the series studied. The remaining lines—drawn as guides for the eyes—join the T_G (upper) and T_C (lower) estimates, and initially appear somewhat different from the essentially triangular structure predicted by both Griffiths' original diluted FM Ising model and the $\pm J$ random bond approach. While these data exhibit scatter around these model-predicted boundaries, what is consistent about such predictions is the narrowing gap *between* T_C and T_G as the Ca doping is increased toward 'optimal' levels, $x = 0.33$. Evidence supporting the narrowing gap between T_C and T_G around $x = 0.25$ can be seen in the data of Belevtsev *et al* [35]. Elements of such scatter are also evident in $La_{1-x}Ba_xMnO_3$ [37], while in $Sm_{1-x}Ca_xMnO_3$ [40] the reported T_G values are neither constant—they decline by some 6% between $x = 0.85$ and 0.92—nor is the corresponding phase diagram reminiscent of the model-predicted forms mentioned above. All of the latter attest to the yet unresolved subtleties displayed by GP-like behaviour in the manganites and its relationship to the emergence of metallicity and CMR.

The resistivity in the PM insulating phase ($d\rho/dT < 0$) are best fitted by the predictions of the adiabatic small polaronic model, within which the associated polaron formation energy exhibits a marked increase across this compositionally modulated M–I boundary.

At compositions above this boundary, the emergence of metallicity is accompanied by CMR which, in model descriptions invoking phase separation, is based on the presence of FM conducting regions embedded in an *AFM insulating* background [5]. It should be noted that the presence of an *FM insulating* phase at compositions below the M–I boundary is not in conflict with such a phase separation

scenario [59, 65]. Ferromagnetism in insulating samples immediately below the M–I boundary results from FM–SE, stabilized by orbital order (OO). The emergence of metallicity is essentially coincident with a transition to an orbitally disordered (OO*) state [59, 65] in which such FM–SE becomes destabilized, being replaced by AFM-SE characteristic of the parent compound, $LaMnO_3$.

Acknowledgments

Support for this work by the Natural Sciences and Engineering Research Council (NSERC) of Canada, the University of Manitoba (in the form of a Fellowship to WJ) and MISIS is gratefully acknowledged.

References

[1] Eerenstein W, Mathur N D and Scott J F 2006 *Nature* **442** 759
[2] Orenstein J and Millis A J 2000 *Science* **288** 468
[3] Wang S and Searle C W 1970 *Can. J. Phys.* **49** 387
[4] Schiffer P, Ramirez A P, Bao W and Cheong S-W 1995 *Phys. Rev. Lett.* **75** 3336
[5] Dagotto E 2002 *Phase Separation and Colossal Magnetoresistance* (Berlin: Springer)
[6] Tokura Y (ed) 2000 *Colossal Magneto-Resistive Oxides* (London: Gordon and Breach) ISBN 90-5699-231-7
Tokura Y and Nagaosa N 2000 *Science* **288** 462
[7] Coey J M D, Viret M and Molnar S V 1999 *Adv. Phys.* **48** 167
[8] Shannon R D 1976 *Acta Crystallogr.* A **32** 751
[9] Rodriguez-Martinez L M and Attfield J P 1996 *Phys. Rev.* B **54** R15622
[10] Anderson P W 1950 *Phys. Rev.* **79** 350
Zener C 1951 *Phys. Rev.* **81** 440
Anderson P W and Hasegawa H 1955 *Phys. Rev.* **100** 675
[11] Tomioka Y, Asamitsu A, Kuwahara H, Moritomo Y and Tokura Y 1996 *Phys. Rev.* B **53** R1689
[12] Okuda T, Tomioka Y, Asamitsu A and Tokura Y 2000 *Phys. Rev.* B **61** 8009
[13] Millis A J, Littlewood P B and Shraiman B I 1995 *Phys. Rev. Lett.* **74** 5144
[14] Moreo A, Yunoki S and Dagotto E 1999 *Science* **283** 2034
Dagotto E 2005 *Science* **309** 257
[15] Salamon M B, Lin P and Chun S H 2002 *Phys. Rev. Lett.* **88** 197203
Salamon M B and Chun S H 2003 *Phys. Rev.* B **68** 014411
[16] Jiang W, Zhou X Z, Williams G, Mukovskii Y and Glazyrin K 2007 *Phys. Rev. Lett.* **99** 177203
[17] Souza J A, Neumeier J J and Yu Y-K 2008 *Phys. Rev.* B **78** 014436
[18] Jiang W, Zhou X Z, Williams G, Mukovskii Y and Glazyrin K 2008 *Phys. Rev.* B **78** 144409
[19] Campostrini M, Hasenbusch M, Pelissetto A, Rossi P and Vicari E 2002 *Phys. Rev.* B **65** 144520
[20] Motome Y and Furukawa N 1999 *J. Phys. Soc. Japan* **68** 3853
Motome Y and Furukawa N 2000 *J. Phys. Soc. Japan* **69** 3785
Motome Y and Furukawa N 2001 *J. Phys. Soc. Japan* **70** 1487
[21] Alonso J L, Fernández L A, Guinea F, Laliena V and Martín-Mayor V 2001 *Nucl. Phys.* B **596** 587
[22] Shulyatev D, Karabashev S, Arsenov A, Mukovskii Y and Zverkov S 2002 *J. Cryst. Growth.* **237–239** 810
[23] Billinge S J L, DiFrancesco R G, Kwei G H, Neumeier J J and Thompson J D 1996 *Phys. Rev. Lett.* **77** 715
[24] Booth C H, Bridges F, Kwei G H, Lawrence J M, Cornelius A L and Neumeier J J 1998 *Phys. Rev. Lett.* **80** 853
[25] Jiang Y, Bridges F, Downward L and Neumeier J J 2007 *Phys. Rev.* B **76** 224428
[26] Božin E S, Schmidt M, DeConinck A J, Paglia G, Mitchell J F, Chatterji T, Radaelli P G, Proffen Th and Billinge S J L 2007 *Phys. Rev. Lett.* **98** 137203
[27] Hennion M, Moussa F, Lehouelleur P, Wang F, Ivanov A, Mukovskii Y M and Shulyatev D 2005 *Phys. Rev. Lett.* **94** 057006
[28] Biotteau G, Hennion M, Moussa F, Rodríguez-Carvajal J, Pinsard L, Revcolevschi A, Mukovskii Y M and Shulyatev D 2001 *Phys. Rev.* B **64** 104421
[29] Dai P, Fernandez-Baca J A, Plummer E W, Tomioka Y and Tokura Y 2001 *Phys. Rev.* B **64** 224429
Dai P, Fernandez-Baca J A, Wakabayashi N, Plummer E W, Tomioka Y and Tokura Y 2000 *Phys. Rev. Lett.* **85** 2553
[30] Markovich V, Jung G, Yuzhelevski Y, Gorodetsky G, Szewczyk A, Gutowska M, Shulyatev D A and Mukovskii Ya M 2004 *Phys. Rev.* B **70** 064414
[31] Markovich V, Fita I, Puzniak R, Tsindlekht M I, Wisniewski A and Gorodetsky G 2002 *Phys. Rev.* B **66** 094409
[32] Adams C P, Lynn J W, Smolyaninova V N, Biswas A, Greene R L, Ratcliff W, Cheong S-W, Mukovskii Y M and Shulyatev D A 2004 *Phys. Rev.* B **70** 134414
[33] Griffiths R B 1969 *Phys. Rev. Lett.* **23** 17
Bray A J 1987 *Phys. Rev. Lett.* **59** 586
Castro-Neto A H, Castilla G and Jones B A 1998 *Phys. Rev. Lett.* **81** 3531
[34] Deisenhofer J, Braak D, Krug von Nidda H-A, Hemberger J, Eremina R M, Ivanshin V A, Balbashov A M, Jug G, Loidl A, Kimura T and Tokura Y 2005 *Phys. Rev. Lett.* **95** 257202
[35] Belevtsev B I, Zvyagina G A, Zhekov K R, Kolobov I G, Yu Beliayev E, Panfilov A S, Galtsov N N, Prokhvatilov A I and Fink-Finowicki J 2006 *Phys. Rev.* B **74** 054427
[36] Jiang W, Zhou X Z, Williams G, Mukovskii Y and Glazyrin K 2007 *Phys. Rev.* B **76** 092404
[37] Jiang W, Zhou X Z, Williams G, Mukovskii Y and Glazyrin K 2008 *Phys. Rev.* B **77** 064424
[38] Jiang W, Zhou X Z and Williams G 2008 *Europhys. Lett.* **84** 47009
[39] Jin C-Q, Zhou J-S, Goodenough J B, Liu Q Q, Zhao J G, Yang L X, Yu Y, Yu R C, Katsura T, Shatskiy A and Ito E 2008 *Proc. Natl Acad. Sci.* **105** 7115
[40] Tong P, Kim B, Kwon D, Qian T, Lee S-I, Cheong S-W and Kim B G 2008 *Phys. Rev.* B **77** 184432
[41] Magen C, Algarabel P A, Morellon L, Araújo J P, Ritter C, Ibarra M R, Pereira A M and Sousa J B 2006 *Phys. Rev. Lett.* **96** 167201
[42] Zhao J H, Kunkel H P, Zhou X Z and Williams G 2001 *J. Phys.: Condens. Matter* **13** 5785
[43] Ju H L, Gopalakrishnan J, Peng J L, Li Q, Xiong G C, Venkatesan T and Greene R L 1995 *Phys. Rev.* B **51** 6143
[44] Stanley H E 1971 *Introduction to Phase Transitions and Critical Phenomena* (Oxford: Clarendon)
[45] Williams G 1991 *Magnetic Susceptibility of Superconductors and Other Spin Systems* ed R A Hein *et al* (New York: Plenum) p 475 et seq
[46] Williams G 2001 *J. Alloys Compounds* **326** 36
[47] Zhao J H, Kunkel H P, Zhou X Z, Williams G and Subramanian M A 1999 *Phys. Rev. Lett.* **83** 219
[48] Li W, Kunkel H P, Zhou X Z, Williams G, Mukovskii Y and Shulyatev D 2004 *Phys. Rev.* B **70** 214413
[49] Ghosh K, Lobb C J, Greene R L, Karabashev S G, Shulyatev D A, Arsenov A A and Mukovskii Y 1998 *Phys. Rev. Lett.* **81** 4740
Kim D, Zink B L, Hellman F and Coey J M D 2002 *Phys. Rev.* B **65** 214424
[50] Kim D, Revaz B, Zink B L, Hellman F, Rhyne J J and Mitchell J F 2002 *Phys. Rev. Lett.* **89** 227202

[51] Li W, Kunkel H P, Zhou X Z, Williams G, Mukovskii Y and Shulyatev D 2007 *Phys. Rev.* B **75** 012406
[52] Arrott A 1957 *Phys. Rev.* **108** 1394
[53] Arrott A and Noakes J E 1967 *Phys. Rev. Lett.* **19** 786
[54] Li W, Kunkel H P, Zhou X Z, Williams G, Mukovskii Y and Shulyatev D 2004 *J. Phys.: Condens. Matter* **16** L109
[55] Shklovskii B I and Efros A L 1984 *Electronic Properties of Doped Semiconductors* (*Springer Series in Solid-State Sciences*) (Berlin: Springer)
[56] Worledge D C, Miéville L and Geballe T H 1998 *Phys. Rev.* B **57** 15267
Ziese M and Srinitiwarawong C 1998 *Phys. Rev.* B **58** 11519
[57] Laiho R, Lisunov K G, Lähderanta E, Stamov V N and Zakhvalinskii V S 2001 *J. Phys.: Condens. Matter* **13** 1233
[58] De Teresa J M, Ibarra M R, Algarabel P A, Ritter C, Marquina C, Blasco J, García J, Del Moral A and Arnold Z 1997 *Nature* **386** 256–9
Souza J A, Terashita H, Granado E, Jardim R F, Oliveira N F Jr and Muccillo R 2008 *Phys. Rev.* B **78** 054411
[59] Jiang W, Zhou X Z, Williams G, Privezentsev R and Mukovskii Y 2009 *Phys. Rev.* B **79** 214433
[60] Kaul S N 1981 *Phys. Rev.* B **24** 6550
[61] Ramakrishnan T V, Krishnamurthy H R, Hassan S R and Venketeswara Pai G 2004 *Phys. Rev. Lett.* **92** 157203
[62] Keffer F 1966 *Spin Waves* (*Handbuch der Physik* vol VIII/2) (Berlin: Springer)
[63] Kittel C 1966 *Introduction to Solid State Physics* 3rd edn (New York: Wiley)
[64] Brown T, Li W, Kunkel H P, Zhou X Z, Williams G, Mukovskii Y and Arsenov A 2005 *J. Phys.: Condens. Matter* **17** 5997
[65] Van Aken B B, Jurchescu O D, Meetsma A, Tomioka Y, Tokura Y and Palstra T T M 2003 *Phys. Rev. Lett.* **90** 066403